The Mars diffuse aurora: a model of ultraviolet and visible emissions

J.-C. Gérard, L. Soret
LPAP, Université de Liège, Belgium

V. Shematovich, D.V. Bisikalo
INASAN, Russian Academy of Sciences
Moscow, Russian Federation

S.W. Bougher
Department of Climate and Space Sciences and Engineering
University of Michigan, Ann Arbor, USA

Keywords: Mars, Aurorae, ultraviolet observations, Aeronomy

Accepted for publication in ICARUS

February 2017

Abstract

A new type of Martian aurora, characterized by an extended spatial distribution, an altitude lower than the discrete aurora and electron precipitation up to 200 keV has been observed following solar activity on several occasions from the MAVEN spacecraft. We describe the results of Monte Carlo simulations of the production of several ultraviolet and violet auroral emissions for initial electron energies extending from 0.25 to 200 keV. These include the CO_2^+ ultraviolet doublet (UVD) at 288.3 and 289.6 nm and the Fox–Duffendack–Barker (FDB) bands, CO Cameron and Fourth Positive bands, OI 130.4 and 297.2 nm and CI 156.1 nm and 165.7 nm multiplets. We calculate the nadir and limb production rates of several of these emissions for a unit precipitated energy flux. Our results indicate that electrons in the range 50-200 keV produce maximum CO_2^+ UVD emission below 75 km, in agreement with the MAVEN observations. We calculate the efficiency of photon production per unit precipitated electron power. The strongest emissions are the CO_2^+ FDB, UVD and CO Cameron bands and the oxygen mission at 297.2 nm. The metastable a $^3\Pi$ state which radiates the Cameron bands is deactivated by collisions below about 110 km. As a consequence, we show that the Cameron band emission is expected to peak at a higher altitude than the CO_2^+ UVD and FDB bands. Collisional quenching also causes the intensity ratio of the CO_2^+ UVD to CO Cameron bands to increase below ~100 km in the energetic diffuse aurora.

1. INTRODUCTION

The Mars ultraviolet aurora was first observed on the Mars nightside with the Spectroscopy for Investigation of Characteristics of the Atmosphere of Mars (SPICAM) UV spectrograph on board Mars Express (Bertaux et al., 2005). Its signature was a sudden increase in the brightness and a change in spectral composition during a limb observation, as the spacecraft was moving along its elliptical orbit near pericenter. The observed spectra changed from a typical NO nightglow caused by radiative recombination of N and O atoms to one resembling the dayside airglow spectrum. During a few seconds, these spectra were dominated by the CO Cameron bands between 190 and 270 nm and the CO_2^+ UV doublet (UVD) at 288.3 and 289.6 nm. Other weak features included OI multiplets and the CO Fourth Positive bands below 170 nm. From the comparison of the time of appearance of the auroral signal in different spatial bins on the detector, the altitude of the observed emission was estimated to be 129±13 km. The same event was re-analyzed by Leblanc et al. (2006) who estimated the brightness of the Cameron and CO_2^+ UVD emissions at about 2.3 and 0.7 kR respectively.

Following this first limb detection, nadir observations were made with SPICAM near Mars Express pericenter. Eight nightside nadir detections on the nightside near regions of crustal magnetic fields were reported by Leblanc et al. (2008). Multiple detections were observed along three orbits. Simultaneous observations identified auroral signatures in measurements made with the Mars Advanced Radar for Subsurface and Ionosphere Sounding (MARSIS) and the Analyzer of Space Plasma and Energetic Atoms (ASPERA-3). They found a very good correlation between the location of the auroral events and regions with a low probability to be on closed crustal magnetic field lines. Leblanc et al. (2008) described in detail two cases of parallel SPICAM and in situ particle measurements. The measured electron precipitation and the aurora appeared closely connected and the total electron content measured with MARSIS was synchronous with the time of the SPICAM auroral detections.

The full SPICAM ultraviolet nightside database was analyzed to identify and characterize auroral detections in the nadir (Gérard et al., 2015) and limb (Soret et al., 2016) directions. In the first study, concurrent electron energy spectra measured in situ with ASPERA-3 were compared with the location of the ultraviolet auroral signatures. It was shown that some distance separated the latitude of the UV auroral signature and the peak of auroral precipitation. This lead Gérard et al. (2015) to conclude that the magnetic field line threading the UV auroral emissions can be inclined by a large angle from the vertical direction. Soret et

al. (2016) used ASPERA-3 in situ electron measurements as an input to a Monte Carlo electron transport by to estimate the expected nadir intensity of the CO Cameron and CO_2^+ UV doublet. The results confirmed that the peak altitude and the order of magnitude of the modeled intensity are correctly predicted. However, the observed brightness is not correlated with the precipitated electron energy flux. Soret et al. (2016) found that the peak altitude of the three events observed at the limb were located at 137 ± 27 km. They showed that this altitude range corresponds to the peak of the energy deposition for electrons in the range 40-200 eV.

Peaked electron distributions have been measured with the magnetometer and electron reflectometer (MAG/ER) on board the Mars Global Surveyor (MGS) satellite (Brain et al., 2006) and by the Analyzer of Space Plasma and Energetic Atoms (ASPERA-3) set of plasma instruments on Mars Express (Lundin et al., 2006). Lundin et al. showed that these electron distributions generally peak at a few hundred eV and may be considered as signatures of acceleration by parallel electric fields along magnetic field lines. They suggested that open magnetic field regions analogous to Earth's polar cusps are often present near strong and moderate crustal fields on the Martian nightside. Brain et al. (2006) reported measurements made on board MGS showing that downward going electrons are generally nearly isotropic for energies between 100 eV and 1 keV. Halekas et al. (2008) described localized events detected in strong magnetic cusp regions that are sometimes associated with signatures of field-aligned currents.

Schneider et al. (2015) discovered a new type of aurora exhibiting drastically different characteristics. The auroral spectra observed with IUVS on board MAVEN on the nightside during this period showed several features similar to these observed with SPICAM with improved spectral resolution and higher sensitivity. The spatial distribution of auroral emissions detected with IUVS spanned ~35° in latitude but did not reach Mars' southern hemisphere. Measurements of the geographic extent of the aurora was limited by the coverage of the observations, so that the aurora was likely even more widespread than the large region covered with IUVS. Limb profiles showed that the emission extended down to ~60 km. The peak brightness of the December 2014 event was close to 70 km, assuming that the emission was horizontally homogeneous. It reached a value of about 400 Rayleighs in the CO_2^+ UVD doublet. They also observed the CO Cameron bands, the OI 297.2 nm OI emission and the short wavelength segment of the CO_2^+ UV-visible Fox–Duffendack–Barker (FDB) bands. The aurorae lasted for several days following periods of solar energetic outbursts.

Simultaneous measurements of energetic electrons with the Solar Wind Electron

Analyzer (SWEA) and Solar Energetic Particle (SEP) instruments indicated that electrons with energies up to 200 keV were causing the observed ultraviolet emissions. They showed a large increase in the measured electron energy flux contemporary, but not exactly in phase, with the diffuse glow observed with IUVS. Unlike the discrete aurora in the southern hemisphere, the presence of emission at all observed locations over 5 continuous days was interpreted as evidence of the absence of substantial patchiness. The consistency of widely separated individual limb scans suggested that projection effects in front of or behind the tangent point of the line of sight are not important.

The 70-km altitude of the emission peak is a clear signature of the presence of highly energetic particles in the precipitated flux. The discrete auroral emissions observed with SPICAM peak ~70 km higher, where the pressure is less by over two orders of magnitude. The diffuse aurora is thus excited by particles penetrating much deeper than the electrons typically causing the discrete aurora. A model of the auroral limb profile was presented by Schneider et al. (2015). They used an analytical fit to the electron energy spectrum detected by SEP and SWEA at 400 km during the December 2014 event. The overall electron number flux distribution approximately followed an $E^{-2.2}$ power law from ~10 to 200 keV. They solved the electron transport equation for energetic electrons to calculate the energy degradation. This electron flux was used to calculate volume emission rates and limb intensity of the CO_2^+ UVD emission. The neutral atmosphere was taken from a mean three constituents (CO_2, N_2, O) Martian neutral atmosphere based on the Mars Climate Database (Millour et al., 2014). They produced a CO_2^+ UVD emission rate profile with a shape matching well the observations. The calculated limb intensity was scaled to match the observed peak brightness measured by IUVS.

In this study, we use a Monte Carlo electron transport model adapted to the Venus (Gérard et al., 2008) and Mars (Shematovich et al., 2008; Soret et al., 2016; Bisikalo et al., 2016) atmospheres to study the vertical and limb intensity of auroral emissions in a CO_2-dominated atmosphere caused by highly energetic electrons. The neutral density altitude distribution including CO_2, CO, O and N_2 densities is given by the M-GITM model (Bougher et al., 2015) adapted to conditions of the IUVS detection of the diffuse aurora. We investigate the variation of altitude of the auroral peak with the electron initial energy. In particular, we investigate the relative importance of processes involving CO_2, CO and O as target species to produce the CO Cameron and Fourth Positive bands, the 130.4 nm and 297.2 nm oxygen emissions and the carbon multiplets at 156.1 nm and 165.7 nm. We also examine the photon production efficiency of emissions produced by a wide range of high electron initial energies.

We then discuss the importance of collisional quenching of the CO ($a^3\Pi$) state that radiates the Cameron bands. Finally, we predict vertically and limb integrated production rates for those emissions expected to dominate the ultraviolet and violet .

2. MONTE CARLO ELECTRON TRANSPORT MODEL

2.1 Numerical method

We use the direct simulation Monte Carlo (DSMC) method to solve the Boltzmann kinetic equation:

$$\mathbf{v}\frac{\partial}{\partial \mathbf{r}} f_e + \mathbf{s}\frac{\partial}{\partial \mathbf{v}} f_e = Q_e(\mathbf{v}) + Q_{e,\mathrm{sec}ondary}(\mathbf{v}) + \sum_{M=CO_2,O,CO,N_2} J(f_e, f_M), \qquad (1)$$

where $f_e(\mathbf{r},\mathbf{v})$, and $f_M(\mathbf{r},\mathbf{v})$ are the velocity distribution functions of the electrons and of the species of the ambient gas, respectively. The left side of the kinetic equation describes the transport of electrons in the Martian gravitational field **s**. In the right-hand side of the kinetic equation, the Q_e term corresponds to the production rate of primary electrons, while the $Q_{e,secondary}$ term describes the rate of formation of secondary electrons. The elastic and inelastic scattering terms *J* for electron collisions with ambient atmospheric species are written in a standard form (Shematovich et al., 1994). It is assumed that the ambient atmospheric gas is characterized by the local Maxwellian velocity distribution functions.

The stochastic solution implies generation of a sample of paths for the state of the physical system including energetic electrons thermalization and transport in the upper atmosphere. The details of the numerical model have been described earlier (Shematovich et al., 1994; 2008). The evolution of the system of test particles caused by collisional processes and particle transport is calculated from the initial to the steady state by solving the Boltzmann kinetic equation. If the collision is elastic, a new pitch angle is randomly assigned to the electron using expressions and parameters developed by Porter and Jump (1978) and Porter et al. (1987) for angular scattering of electrons. For inelastic collisions, we use the forward scattering approximation above 100 eV. It is assumed that the differential cross section for these collisions is so strongly peaked in the forward direction that angular redistribution by this process is negligible. If the collision produces ionization, a secondary electron is created, and an isotropically distributed pitch angle is randomly assigned as well as an updated energy value. When a steady state is reached it is possible to accumulate the

statistics with the needed accuracy.

We assume that the ambient atmospheric gas is characterized by local Maxwellian velocity distribution functions. In order to minimize boundary effects, the lower boundary was set at an altitude of 50 km, and the upper boundary was fixed at 300 km. The pitch angle distribution is assumed to be isotropic at the top of the model. The elastic and inelastic scattering terms for electron collisions with the ambient atmospheric species are written in the standard form (Shematovich et al., 1994). The relative importance of the collisional processes slowing down the electrons is governed by their cross sections. The list of cross sections used to calculate energy degradation along the path of the test electrons and further details on the Monte Carlo model were given by Shematovich et al. (2008) and will be presented and updated in section 2.3.

2.2 Model atmosphere

We use the CO_2, CO, O Ar and N_2 density profiles calculated by the Mars Global Ionosphere-Thermosphere Model (M-GITM) (Bougher et al., 2015). The CO_2 and N_2 density profiles simulated by M-GITM match reasonably well the in situ measurements made during the MAVEN Deep Dip #2 campaign down to ~150 km (Bougher et al., 2015b) on the dayside. For example, between 160 and 220 km, M-GITM diurnal variations of CO_2 encompass NGIMS densities quite well, whereas below 160 km, M-GITM underestimates NGIMS the CO_2 densities by up to a factor of ~2 at 130 km. The atomic O scale height does not follow this pattern of transitioning scale heights because local chemical production and loss processes also control this chemically active species. For these model calculations, we use the density and temperature profiles from M-GITM close to the conditions prevailing during the December 2014 event: local time = 24:00, latitude = 62.5° N, Ls= 270°, F10.7 solar flux index = 160 (at Earth). Figure 1 shows the corresponding CO_2, CO and O density profiles. The temperature at 300 km is 139 K and a change of atmospheric scale height is observed near 120 km where the temperature starts increasing with altitude. This cold nightside topside temperature is similar to that observed by the MRO Accelerometer during aerobraking deep on the nightside and near the equator (Keating et al. 2008; Bougher et al., 2016).

We note that the temperature and density model used in this study is quite different from that used by Schneider et al. (2015) which was a global mean Martian neutral atmosphere (consisting of CO_2, N_2, and O) based on the Mars Climate Database (Millour et al., 2014). The exospheric temperature in their model was 250 K, which caused the density

profiles to differ from the M-TIGCM values. The CO_2 density is similar (within a factor of 2 or less) below 150 km, but significantly less at high altitude (by four orders of magnitude at 300 km) in the M-GITM. The nighttime O density is higher in the M-GITM than in the global model over most of the altitude range, causing the crossing point with the CO_2 density curve to be located near 150 km, significantly lower than on dayside.

2.3 Excitation processes and relevant cross sections

The list of excitation processes leading to emissions and the adopted cross sections are described in Table 1. Most of them are used in the analytic form given in the critical review by Shirai et al. (2001) who compared and discussed the sources of their adopted values. Some others were (re)measured following their work and have been used in numerical form as mentioned in the Table and discussed in this section.

Two major emissions from excited CO_2^+ ions arise from electron impact on CO_2 molecules. First, the doublet at 288.3 nm and 289.6 nm of B $^2\Pi_u \rightarrow$ X $^2\Pi_u$ transition is a dominant feature of the auroral spectra observed by Schneider et al. (2015). The threshold for excitation is 17.3 eV and the electron impact cross section peaks at 165 eV. Second, the CO_2^+ $A^2\Pi \rightarrow X\ ^2\Pi_u$ transition generates the FDB bands extending from the ultraviolet to the blue part of the spectrum. They were first observed by Barth et al. (1971) in the Mars dayglow and are expected to be an important component of the Mars auroral spectrum (Lilensten et al., 2015).

The CO Cameron bands arise from the dipole spin-forbidden $a^3\Pi \rightarrow X^1\Sigma$ transition and are the brightest features in the Martian ultraviolet dayglow. The CO ($a^3\Pi$) upper state of the Cameron bands is both directly excited by electron impact from the CO2 and CO ground states and indirectly by internal cascades between the excited CO electronic states. It is populated by electron bombardment on CO_2 with a threshold at 11.5 eV, but electron impact on CO molecules can also make a substantial contribution (threshold: 6 eV). The corresponding cross sections for electron impact on CO_2 and CO peak around 80 eV and 11 eV respectively. Since the CO ($a^3\Pi$) molecules are dissociative fragments of CO_2, they carry excess kinetic energy and such excited molecules can escape from the excitation region in the laboratory. Laboratory measurements by Erdman and Zipf (1983) concluded that the cross section measurement by Ajello et al. (1971a) was flawed and revised the peak value from $1x10^{-17}$ to $9x10^{-17}$ cm^2. They subsequently multiplied this value by a factor of 2.7 to account for

higher mean velocity of CO ($a^3\Pi$) fragments, which might have escaped detection. Bhardwaj and Jain (2009) and Jain and Bhardwaj (2012) used their value in the analysis of the Mars ultraviolet dayglow. Models comparisons with Mars dayglow observations with SPICAM suggest that this value produces too high Cameron intensities (Shematovich et al., 2008; Simon et al., 2009; Jain and Bhardwaj, 2012; Gronoff et al., 2012). These studies recommend that the Cameron band cross sections of Erdman and Zipf (1983) should be reduced by a factor of 2 to 3, to bring the calculated intensities into agreement with the SPICAM observations. Following these results, re-evaluation of the radiative lifetime of the $a_3\Pi$ state, and discussions by Furlong and Newell (1996), Itikawa (2002) and Gronoff et al. (2012), we scale the Cameron system emission cross-section to the peak value of $8x10^{-17}$ cm^2 at 80 eV. This value is close to $7x10^{-17}$ cm^2, deduced by Conway (1981) from his analysis of the Martian dayglow. Considering the complexity of the laboratory measurements, we estimate the uncertainty on the absolute cross section to be at least a factor of 2.

The CO Fourth Positive system arising from the allowed $A^1\Pi \rightarrow X^1\Sigma$ transition extending from ~125 to 170 nm was also observed in SPICAM spectra of the discrete aurora. As the Cameron bands, this emission is excited by electron impact on both CO_2 (threshold: 13. 5 eV) and CO molecules (threshold: 8 eV, peak: 23 eV). The analytical cross section by Shirai (2001) has been scaled up by a factor of 1.4 to match the experimental determination of the total emission cross section (including cascades) by Beegle et al. (1999).

Atomic oxygen emissions have been observed in the discrete aurora (Bertaux et al, 2005; Soret et al., 2016) and are expected in the diffuse aurora. The O $^1S \rightarrow {}^3P$ transition at 297.2 nm is also weakly present in the spectrum of diffuse aurora observed with IUVS. This forbidden emission has the same upper level as the green line at 557.7 nm. The combination of excitation cross sections for processes 12, 13 and 14 with the relative abundance of CO_2, CO and O, indicate that electron impact on CO_2 dominates over the other two processes. O(^1S) radiative transitions to the ^1D and ^3P levels give rise to the green line at 557.7 nm and 297.2 nm emission respectively. In the absence of measurement or reliable prediction of the electron and O_2^+ densities at low altitude in regions of diffuse auroral precipitation, we do not account for the $O_2^+ + e \rightarrow O(^1S) + O$ dissociative excitation. In addition, the quantum yield of the recombination process is still uncertain (between 3 % and 7%) and the reaction rate depends on the unknown electron temperature under auroral conditions. Other potential processes such as collisions between metastable N_2 ($A^3\Sigma$) metastable molecules with O or $O_2^+ + N \rightarrow NO^+ + O(^1S)$ charge transfer are not included in these model calculations. The

relative importance of these sources was shown to be secondary compared to other processes in the Martian dayglow (Gronoff et al., 2012). Therefore, in this study we solely consider processes 12, 13 and 14 as sources of O(^{1}S) metastable atoms and our O(^{1}S) calculated production rate is probably a lower limit. Since the O(^{1}S) state radiates through the 557.7 nm multiplet to the O(^{1}S) state and 297.2 nm to the O(^{3}P) states, one needs to know the branching ratio between the two emissions. The 557.7-nm/297.2-nm ratio of Einstein coefficients recommended by NIST is 16.4, but this value is in disagreement with recent atmospheric observations. Therefore, we adopt a ratio of 9.5 that is midway between the night airglow measurement of 9.8±1.0 by Slanger et al. (2006) and the auroral value of 9.3±0.5 derived by Gattinger et al. (2009) respectively. It is nearly half the value recommended by NIST based on quantum mechanics calculations.

The 103.4 and 135.6 nm multiplets are excited by electron collisions with O atoms, CO_2 and CO molecules. The cross section for the e + CO source for the 135.6 nm emission has been measured in absolute units by Ajello et al. (1971b), while the value for the e + CO_2 collisions was only given in arbitrary units by Ajello et al. (1971a). Therefore, in the absence of absolute value for the e + CO_2 cross section, we do not calculate the source of auroral 135.6 nm emission at this point.

The cross sections for electron impact on CO_2 and CO to produce the O (^{3}S) upper state of the 130.4 nm emission were measured by Ajello (1971, a, b) and Mumma et al. (1972). The two sets of cross sections measured for this emission show differences with each other. Mumma et al. normalized their cross section to that for Lyman-α emission produced by electron impact on H_2. In his review of excitation cross sections, Itikawa (2002) indicates that if an updated Lyman-α excitation cross section is employed for normalization, the values of Mumma et al. should be multiplied by 0.61. We have applied this correction in the following calculations. The relative importance of the e + O and the e + CO_2 processes as sources of O(^{1}S) atoms depends on the O mixing ratio and thus varies with altitude. It is likely that the CI multiplets at 156.1 and 165.7 nm are also present, although no positive detection was confirmed by the analysis of SPICAM auroral spectra (Bertaux et al., 2005; Leblanc et al., 2006; Soret et al., 2016).

3. MODEL SIMULATIONS

We now describe the results of model simulations for monoenergetic precipitation. We first illustrate the interaction of the auroral electron beam with the Martian atmosphere. We

then describe production rates of different emissions for the 100-keV case and their variations as a function of the incident electron energy. Finally, we discuss the role of collisional quenching and provide vertically integrated emission rates.

3.1 Electron energy degradation

As they interact with the Martian neutral atmosphere, the high energy incident electrons create a multitude of secondary electrons at lower energies, which efficiently interacts with the local gases to cause further ionization and excitation. Bisikalo et al. (2016) showed that the presence of the crustal and induced magnetic field increases the ratio of the upgoing to the downgoing electrons flux as mirroring electrons add up to the collisionally backscattered electrons following stochastic scattering. However, as the electrons spiral down toward the atmosphere, the intensity of the crustal field increases and the area of the flux tube decreases. Consequently, the two effects compensate each other and the emission rate (expressed in Rayleigh units) remains essentially unchanged. In addition, the reported occurrence of diffuse aurora is so far limited to the northern hemisphere where the crustal magnetic field is quasi absent. In the following numerical simulations, we do not consider the effect of a magnetic field.

Only a sufficiently "hard" electron energy distribution, with substantial fluxes of electrons of energies above ~50 keV, can create a peak at 70 km as was observed with IUVS in the diffuse aurora. As the electron beam penetrates into the atmosphere, they progressively yield their energy by elastic and inelastic ionization collisions, optical emissions and neutral gas heating. The descending energy flux slowly decreases in the upper rarified atmosphere until the pressure increases and the electrons deposit most of their energy. Ultimately, the energy flux drops to zero and no emission is produced below this altitude. This is illustrated in Figure 2 showing the descending energy flux versus altitude for a monoenergetic precipitation of 100 keV electrons. At the top of the model, the downward flux is 1 mW m^{-2}, the value of the total injected power per unit area. It progressively decreases until it reaches 100 km and subsequently rapidly drops to much smaller values, reflecting the strong interaction with the atmospheric gas in this altitude range.

In Figure 3, the calculated shape of the electron energy spectrum is shown for three altitudes on a double logarithmic scale in electrons in units of cm^{-2} s^{-1} eV^{-1}. The top one is located above most of the interaction region. It shows that, at high altitude, the primary precipitating electrons are only weakly attenuated and form a peak close to the 100 keV initial

energy. The relatively small amount of secondary electrons formed during the ionization processes populates the low energy part of the spectrum. A gap between primary and secondary electrons is therefore clearly present. The second panel shows the distribution at 131 km, above the region of the bulk energy deposition. As altitude decreases, the number of collisions increases and a thermal peak appears near 8 eV, followed by a drop toward higher energies. The attenuated primary electrons progressively loose their energy and progressively populate the gap from the high energy side, leading to the appearance of a large population of secondary electrons. These, in turn, populate the gap from the low energy side. As a consequence, these two processes fill the energy gap, and a well defined high energetic tail forms between a few keV up to ~100 keV. The bottom panel shows the calculated energy spectrum at 81 km, close to the peak of the ultraviolet emissions where the number of collisions is considerably higher. The flux below 10 eV is then nearly identical to its value at higher altitude. However, it quickly drops beyond ~10 eV. The high energy tail is still largely unaffected and the lower energy range still corresponds to a mixture of degraded primary and secondary electron populations.

3.2 Model simulations: 100 keV monoenergetic electrons

To evaluate the relative importance of the source processes listed in Table 1, we now examine the volume production rate and the limb integrated production rate for a monoenergetic electron precipitation of 100 keV electrons. For this purpose, we use the steady state electron energy spectra calculated at each vertical grid point folded with the excitation cross section for a series of expected emissions.

The electron energy spectra calculated in each vertical cell of the Monte Carlo transport model are then folded with the corresponding excitation cross section to calculate volume production rates as a function of altitude. The CO_2^+ UV doublet at 288.3 and 289.6 nm is only excited by process (1) (Table 1). Its volume production rate shows a peak of 127 photons cm^{-3} s^{-1} at 66 km and drops with a scale height of 14 km up to ~110 km (not shown). At higher altitude, the emission scale height decreases to about 7 km up to the top of the model. This change of scale height reflects the CO_2 density profile (Figure 1) and its inflexions related to the vertical temperature distribution. The production rates of the CO Cameron bands and the OI 130.4 nm triplet emissions are illustrated in Figure 4a and 4b

respectively. The production rate vertical distribution is shown in panel (a) for processes (3) and (4), the two known sources of the CO (a $^3\Pi$) state. Electron impact on CO_2 molecules remains the dominant source up to 180 km, but e + CO collisions also contribute to the total production. As expected from Figure 1, the relative importance of the two sources changes with altitude, as a consequence of the increase of the CO mixing ratio with altitude in the neutral model. Their e + CO source peaks 17 km higher than the e + CO_2 source. Integrated over the vertical column, it contributes 8 % of the total production. The overall peak altitude is 66 km with a total production rate of 196 photons cm^{-3} s^{-1}. Panel (b) illustrates the VER of the 130.4 nm triplet production from processes (7) and (8). The e + CO_2 source is dominant and peaks 8 km lower than the e + O production. It contributes 77 % to the total column production rate of the upper state of the 130.4 nm triplet. As will be discussed later, absorption by CO_2 is important over most of the emission profile to 110 km, so that the contribution of process (7) to the emergent intensity may be important.

The altitude dependence of other auroral emissions presented in Figure 5 shows similar results when compared with the results for the CO Cameron bands and the CO_2^+ UVD bands. The peak VERs of the auroral emissions ranges over about four orders of magnitude. The brightest emissions are the CO_2^+ Fox–Duffendack–Barker and UVD bands, the CO Cameron bands, and the OI forbidden emission at 297.2 nm. The CO_2^+ FDB bands closely track the emission profile of the CO_2^+ UVD and become dominant at lower altitude. The CO_2^+ UV doublet whose peak production rate is about three times less than the FDB emission is the third dominant emission.

A second series of emissions shows a peak nearly two orders of magnitude weaker than the first group. It includes the CO Fourth Positive bands and the 130.4 nm triplet, followed by the carbon emissions at 156.1 and 165.7 nm. The CO 4P profile shows a somewhat different shape and peak altitude than the Cameron and CO_2^+ UVD bands. Detailed examination reveals that these differences are caused by the important role played by the e + CO process (labeled 6 in Table 1) as a source of CO (A) excitation relative to e + CO_2 (process 5). Integrated over the total vertical column, electron impact on CO contributes about 40% of the total CO A state production, compared to 0% for the CO_2^+ UVD emission and 8% for the Cameron bands.

The two neutral carbon multiplets are excited by processes (15), (16) and (17). The contribution of direct electron impact on C atoms (13) is based on the C density profile calculated by Fox (2004) for high solar activity. Detailed calculations show that process (15) dominates over the other two sources by more than two orders of magnitude.

3.3 Model simulations: dependence on electron energy

Volume production rates have been calculated for a wide range of monoenergetic initial energies of the incident auroral electrons. Examples for the CO Cameron and the CO_2^+ UV doublet are shown in Figure 6. Curves for electron energies less than 1 keV were given by Soret et al. (2016) for a somewhat different neutral atmospheric model as discussed in the introduction. They were intended to model ultraviolet emissions generated in the discrete aurora. The altitude of the emission peak of the CO_2^+ UVD shown in panel (a) steadily decreases with increasing initial electron energy. It ranges from 147 km for 250 eV, to 106 km for 10 keV and 51 km for 200 keV electrons. Interestingly, the value of the maximum volume emission rate also decreases as the electron energy increases beyond 1 keV, although the total energy input at the top of the model remains equal at 1 mW m^{-2}. It drops by about one order of magnitude between 100 eV and 100 keV, whereas the width of the distribution slightly increases with the electron energy, reflecting the change in atmospheric scale height.

The altitude and peak values of the Cameron bands (panel b) show a similar but not identical dependence on electron energy. The differences in shape between the two emissions are more pronounced at high energy when the electrons reach down regions below 100 km. The relative abundance of CO then rapidly drops below 10% and makes process (4) become progressively negligible relative to (3) as may be seen in Figure 4a.

3.4 Vertical and limb integration

The volume production rates shown in Figure 5 have been integrated along the line of sight to determine the vertically and limb integrated production rates for a wide range of electron energies assuming a 1 mW m^{-2} electron precipitation.

In agreement with Figure 6, for mean electron energies between 100 and 200 keV encountered in the diffuse aurora, a first group of relatively large vertical integrals are associated with the CO_2^+ FDB, the CO Cameron and the CO_2^+ UVD bands and the OI 297.2 nm emissions. The CO 4th Positive bands, the OI 130.4 nm and the CI integrated values are significantly weaker. These vertically integrated production rates are listed in Table 2. These integrated quantities will differ from the nadir intensity if the upper state of the transition is collisionally quenched, is self absorbed or absorbed by the neutral gas or feeds another transition. These include the CO_2^+ UVD and FDB systems, the CO 4P bands, and the CI lines.

The role of collisional quenching of metastable CO (a $^3\Pi$) and O(^{1}S) states will be discussed in sections 3.5.1 and 3.5.2. Therefore, the numbers in Table 2 are not all equal to the emerging intensity as some of these emissions are partly absorbed by CO_2 along the photon path or backscattered by the underlying atmosphere. This is the case for OI 130.4 and 135.6 nm and, to a lesser degree for the CI 156.1 and 165.7 nm emissions, when electrons penetrate deep enough to reach regions where absorption at the relevant wavelengths becomes significant. For example, unit vertical optical depth for absorption by CO_2 is reached near 110 km at 130.4 nm in the model atmosphere adopted here. Consequently, a part of the emitted photons is absorbed in the case of electron precipitation carrying electrons exceeding a few keV. In addition, multiple scattering will further complicate radiative transfer within the three-multiplet components of the 130.4 nm emission (Thomas et al., 1971; Strickland et al., 1972) and CO 4P bands. This question will need to be quantitatively addressed if further observations make it possible to measure the altitude distribution of the 130.4 nm emission in the Martian diffuse aurora.

We then integrate the volume production rate presented in the previous sections along the line of sight at the limb. We assume that the aurora is widespread and horizontally quasi-homogenous as was suggested by the IUVS observations in the diffuse aurora. We do not account here for the possible smoothing effect of the emission profile by the finite field of view of the observing instrument. Figure 7 presents calculated limb profiles of the CO_2^+ UVD and CO Cameron bands following integration of the volume production rates shown in Figure 6. Values are expressed in Rayleighs (= 10^6 photons/cm^2 s in 4π steradians), but they refer to the slant integral of the photon production, neglecting for the moment quenching of the CO a state. The calculated shape of the Cameron band curves and their dependence on electron energy are very similar to those for the CO_2^+ UVD emission. However, the Cameron limb intensities are higher by a factor decreasing from ~4 at 100 eV to nearly ~2 at 200 keV.

Comparison of the results in Figure 7a with the CO_2^+ UVD limb profile shown in Schneider et al. (2015)'s in Figure 4 indicates that the observed peak between 70 and 75 km approximately corresponds to the peak altitude of 72 km for a ~60 keV monoenergetic electron precipitation. The electron spectrum measured with the SEP and SWEA instruments during the December 2014 diffuse auroral event was not monoenergetic but was approximated by an $E^{-2.2}$ energy dependence between 0.1 and 200 keV.

3.5 Collisional quenching of metastable states

Competition between radiation and collisions needs to be accounted for to model the expected Cameron band and OI 297.2 nm intensities when auroral electrons penetrate in the Martian atmosphere deeper than the discrete aurora.

3.5.1 Cameron bands

Since the CO a $^3\Pi \rightarrow X\ ^1\Sigma$ transition in the CO molecule is forbidden by the $\Delta S=0$ spin rule, the CO ($a^3\Pi$) metastable upper state may suffer collisional deactivation. It is quenched by thermal collisions with CO_2 and CO Its radiative lifetime τ is difficult to measure experimentally and depends on the value of the J rotational level. Measured values have yielded values between 1.0 (Borst and Zipf, 1971) and 7.5 ms (Lawrence, 1971). James (1971) noted that the Einstein coefficients of the different (0,v") Cameron bands strongly vary with the J rotational quantum number. In a situation of rapid equilibration of population between the various rotational components, he calculated τ = 8.75±1 ms for the average lifetime. Slanger and Black (1971) combined quenching rate coefficients, populating transitions and Cameron band intensities to determine a global average lifetime of 4.4±1.1 ms. Jongma et al. (1997) used two different techniques to determine a lifetime of 3.6±0.17 ms for the J=1 doublet. Gilijamse (2007) combined experimental and theoretical approach and obtained a value of τ = 2.63±0.03 ms for the v=0, J=1 level. Based on the sum of the $A_{0,v"}$ values given by Jongma et al. (1997), we obtain an average radiative lifetime for the Cameron bands of 3.6 ms, which we adopt as our central value. We explore the sensitivity of the Cameron bands intensity to this quantity by varying the lifetime from 1.0 to 7.5 ms.

Several laboratory determinations of the CO ($a^3\Pi$) + CO_2 quenching coefficient have been made since the first laboratory measurement by Lawrence et al. (1971). Measured values vary from $1.2x10^{-11}$ (Lawrence et al., 1971), $1.7x10^{-11}$ (Slanger and Black, 1971), $2.0x10^{-11}$ (Taylor and Setzer, 1973), up to $4.8x10^{-11}$ cm^3 s^{-1} (Wauchop and Broida, 1973). We use the mid-range value of $k_{CO2} = 2.0x10^{-11}$ cm^3 s^{-1} with minimum and maximum values of $1.2x10^{-11}$ and $4.8x10^{-11}$ cm^3 s^{-1} respectively. Measurements of the quenching coefficients by CO molecules have been reviewed by Wysong (2000). They range from $5.7x10^{-11}$ to $1.2x10^{-10}$ cm^{-3} s^{-1}. We adopt an intermediate value $k_{CO}= 1x10^{-10}$ cm^3 s^{-1} with extreme values of $5.7x10^{-11}$ to $1.2x10^{-10}$ cm^{-3} s^{-1}.

At a given altitude, the ratio R(z) of the volume emission rate to the production rate is given by:

$$R(z) = \{1 + \tau(k_{CO2}[CO_2] + k_{CO}[CO])\}^{-1} \quad (2)$$

where $[CO_2]$ and [CO] are the local densities of CO_2 and CO molecules.

Values of R(z) decrease from 1 above 120 km, to 0.83 at 100 km, 0.30 at 80 km and 0.05 at 60 km. Therefore, below 110 km, the volume emission rate becomes progressively smaller than the production rate of the CO ($a^3\Pi$) state that was shown in Figure 4. Consequently, the volume emission rate of the Cameron bands for a 100 keV electron precipitation steadily decreases below about 110 km and becomes vanishingly small below 70 km. The simulated limb profile in Figure 8a illustrates the role of collisional deactivation on the limb profile of the Cameron bands. The unquenched and the quenched emission rates significantly depart below about 100 km. The relatively large residual Cameron intensity far below the emission peak is caused by the contribution along the line of integration at the limb of the emitting layers located at higher altitude. Consequently, the decrease in limb intensity does not exceed a factor of 6, in spite of the large drop in the volume emission rate caused by quenching at low altitude.

Consideration of collisional deactivation of the CO ($a^3\Pi$) state significantly modifies the peak altitude of the Cameron bands which is raised up by 5 to 40 km in the case of a 100 keV electron precipitation depending on the set of parameters used in the above relation for R(z). The dashed lines show the range of values stemming from the uncertainties on the radiative lifetime and the quenching coefficients of the CO ($a^3\Pi$) state. The emission rate near the emission peak at 75 km decreases by as much as a factor of ~8 if the longest radiative lifetime and the largest quenching coefficients are used in the simulations. The uncertainty on the radiative lifetime ranges from 1.0 to 7.5 ms and produces most of the difference between the maximum and minimum dashed curves. The values of k_{CO2} and k_{CO} are varied between 1.2 and 4.8×10^{-11} cm^3 s^{-1} and 7.6 to 12×10^{-11} cm^3 s^{-1} respectively.

Figure 8b simulates a comparison between the emissions rates of the permitted CO_2^+ UV doublet and the CO Cameron emissions. The ratio of the two intensities is calculated with and without quenching. As expected, the CO/CO_2^+ intensity ratio decreases under the effect of collisions down to 60 km and nearly stabilizes at lower altitude. This stems from the fact

that, below the emission peak, the upper layers make the dominant contribution to the line of sight integral. It is therefore expected that the CO Cameron/CO_2 UVD limb intensity ratio of the two emissions will decrease for observations of aurora excited by electrons with highly energetic electrons. Emission curves shown in Figure 6b suggest that deactivation affects the auroral spectral distribution for energies exceeding 5-10 keV. One should also note that the intensity ratio of the two emissions varies in the absence of quenching. It drops from about 4.4 near 120 km to 2 near the emission peak. This variation is a consequence of the altitude dependence of process (4) relative to (3) and changes in the shape of the electron energy spectrum with altitude. It is important to remember that the CO/CO_2^+ intensity ratio also depends on the relative cross sections of processes (1), (3) and (4), whose exact values are uncertain.

When quenching is considered, the calculated ratio between the Cameron bands and the CO_2^+ UVD at the limb is on the order of 4.5 above 120 km and decreases at lower altitude. This value is in reasonable agreement with the ratio SPICAM observations of the discrete aurora reported by Soret et al. (2016) and the MAVEN-IUVS value observed in the Martian dayglow. These results suggest that CO_2^+ emission limb profiles should be used as an indicator of the electron energy deposition versus altitude in the Martian diffuse aurora rather than the CO Cameron bands.

3.5.2 OI 297.2 nm

The O (^{1}S) level has a radiative lifetime of 0.77 s and is therefore also susceptible to be deactivated by collisions with ambient atoms and molecules atoms at sufficiently low altitude. We adopt the following quenching coefficients:

CO_2: 3.2×10^{-11} exp(-1323/T) $cm^3\ s^{-1}$ (Capetanakis et al., 1993)
CO: 7.4×10^{-14} exp(-957/T) $cm^3\ s^{-1}$ (Capetanakis et al., 1993)
O: less than 1.2×10^{-14} $cm^3\ s^{-1}$ (Slanger and Black, 1981)
N_2: < 2×10^{-17} $cm^3\ s^{-1}$ (Atkinson and Welge, 1972)

The net volume emission rate is calculated using equation (2) where the lifetime and quenching coefficients have been adapted to the O(^{1}S) state. Calculations indicates that only deactivation by collisions with CO_2 is important, as the quenching coefficients for O, CO are low compared to those for CO_2 and involve minor constituents as collision partners.

Quenching by N_2 is negligible since both the rate coefficient and the N_2 mixing ratio are small. We note that quenching of the (^{1}S) state at low altitude increases the emission peak altitude and decreases the vertically integrated emission rate compared to simulations when quenching is neglected.

Although the ^{1}S to ^{1}D transition at 557.7 nm has not been measured in the diffuse aurora, its emission profile can be directly obtained by multiplying the 297.2 nm values by the ratio of the transition probabilities (9.8 in this study).

4. EFFICIENCY OF PHOTON PRODUCTION

As shown in Figure 5, the different emissions show, as expected, a widely different production rate profile for a given electron precipitation. In Figure 9, we examine the response of each individual emission feature to precipitation characterized by different electron energies. This plot was obtained by vertically integrating all volume emission rates for a range of initial electron energies between 0.1 and 200 keV. Some of these values differ from those given in Table 2 since the effect of collisional deactivation of the CO ($a^3\Pi$) and O(^{1}S) states is accounted for, as described before. The adopted set of lifetime and quenching coefficients consists in the mid-range values described in section 3.5.1 for the CO ($a^3\Pi$) state and those listed in section 3.5.2 for O(^{1}S) deactivation. Some general comments may be formulated from the comparison between the different curves.

The energy dependence of emission efficiency results from the competition between excitation of electronic states and other competing energy loss processes such as ionization or molecular dissociation. It also depends on the atmospheric composition and the shape of the excitation cross section for each specific emission. Emission efficiencies (emergent intensity divided by the initial energy flux) generally show a decreasing trend with increasing electron energy. The photon production efficiency of the CO Cameron and Fourth Positive bands, the OI 130.4 nm and CI emissions monotonically decreases with increasing electron energy from 0.1 to 200 keV. The CO_2^+ UVD and FDB bands, the OI 297.2 nm and 130.4 nm emissions first show a small increase above 0.1 keV, followed by a decrease of the emission efficiency. The efficiency of the Cameron bands, which dominates over the CO_2^+ FDB and UVD bands for electron energies below 5 and 30 keV respectively, progressively decreases with increasing energy in such a way that the CO_2^+ band systems become dominant at high energies. At 200 keV, the Cameron/UVD intensity ratio is close to 0.6, by contrast to the ratio of 6.1 at 100 eV. As discussed in section 3.6, this is the result of the increasing importance of

collisional quenching of the CO a state as the electrons penetrate deeper into the Martian atmosphere. We also note that the CO_2^+ FDB band intensity remains quasi parallel to the CO_2^+ UVD. This is explained by the common source molecule (CO_2) and the similarity of the energy dependence of the two excitation cross sections. Similarly, the two carbon emission efficiencies remain in a constant ~2 intensity ratio for the same reason.

5. DISCUSSION

The altitude of the CO_2^+ emission peak is a sensitive remote sensing indicator of the characteristic energy of the precipitation. The Monte Carlo numerical simulations predict a CO_2^+ UVD emission peak varying between 150 and 50 km for monoenergetic electron precipitation ranging from 250 eV to 200 keV. The CO_2^+ Fox–Duffendack–Barker and UV doublet band systems are among the brightest emissions predicted in our study. Some of the FDB bands have been observed in the Martian dayglow with the Mariner UV spectrometers (Barth et al., 1971). Our calculations indicate that their limb profile should be very similar to that of the CO_2^+ UVD. The CO Fourth Positive bands are also within the range of IUVS instrument and should be detectable. However, for this transition a band by band study is required as i) the short wavelength bands might be significantly absorbed by CO_2 and ii) the (v',0) bands may be optically thick, depending on the altitude of the emission. A similar situation was observed in the Mars and Venus dayglow (Feldman et al., 2000; Hubert at al., 2010) who used optically thin transitions to estimate the CO column abundance. We note that the importance of the difference emission sources directly depends on the thermal profile and chemical composition of the Martian upper atmosphere. The values given in this study are based on the current version of the M-GITM model for conditions prevailing in December 2014 in the northern hemisphere. Actually, they may vary depending on season, latitude, and solar activity. Their altitude distribution and relative importance will adjust accordingly.

The measured brightness of the OI 130.4 and 135.6 nm multiplets in the diffuse aurora may be strongly reduced by absorption by CO_2 whose cross section varies from 1.1 and 0.8×10^{-18} cm^2 between 130.2 and 130.6 nm and 6×10^{-19} cm^2 at 235.6 nm (Yoshino et al., 1996). The corresponding unit vertical optical depth level in the atmospheric model is reached near 110 km, so that the emerging intensity in the diffuse aurora is expected to be very low, especially when observed at the limb. In addition, the resonance OI 130.4 nm triplet is partly self-absorbed and a detailed radiative transfer calculation is needed to convert the volume emission rate vertical distribution into a limb profile (Thomas, 1971; Strickland et al., 1972).

Our study also shows that quenching of auroral events will indicate the range of Cameron/CO_2^+ UVD ratio values observed below ~100 km, in the the CO (a) state modifies the altitude of the emission peak of the Cameron bands. The higher the electron energy the largest the difference will be between the altitude of the maximum emission of the Cameron and the CO_2^+ UVD and FDB bands. Analysis of the IUVS spectra observed during several diffuse region of expected significant quenching of the CO ($a^3\Pi$) state. Detailed comparisons with observed limb profiles will also help to validate or not the set of quenching parameters used in this study. Future work will also provide comparisons between observed limb profiles of several spectral features measured in different diffuse auroral events with intensities calculated using the combined electron energy fluxes simultaneously measured in situ with the SWEA and instruments. In particular, the altitude dependence of the Cameron/CO_2^+ UVD ratio will help quantify the importance of collisional quenching of the CO ($a\ ^3\Pi$) state.

As mentioned in section 3.4, some of the excitation cross sections are uncertain. In particular most laboratory measurements are limited to electron energies of 1 keV or less. In this study, we extended the values at highest available energy using a 1/E dependence, which may introduce significant uncertainties in some of the estimated production rates for the highly energetic electron precipitation encountered during the diffuse aurora. Further experimental work to extend the range of measured cross sections is clearly needed. It is also expected that future detailed observations of the absolute and relative brightness of several features of the diffuse aurora will help reducing these uncertainties.

Acknowledgements. This research was partly funded by the CODYMAV PRODEX program managed by the European Space Agency with help of the Belgian Science Policy Office(BELSPO) and by BELSPO's SCOOP/BRAIN research contract. D.B. and V.S. acknowledge financial support by the Russian Science Foundation (Project nr. 14-12-01048). We thank both reviewers for their useful comments.

References

Ajello, J.M. (1971a) Emission cross sections of CO_2 by electron impact in the interval 1260–4500 Å. II. J. Chem. Phys. 55, 3169–3177.

Ajello, J. M. (1971b). Emission Cross Sections of CO by electron impact in the interval 1260-5000 Å. I. J. Chem. Phys. 55, 3158-3168.

Atkinson, R., and Welge, K. H. (1972), Temperature dependence of O(^{1}S) deactivation by CO_2, O_2, N_2, and Ar. J. Chem. Phys., 57, 3689–3693.

Barth, C. A., Hord, C. W., Pearce, J. B., Kelly, K. K., Anderson, G. P., and Stewart, A. I. (1971), Mariner 6 and 7 ultraviolet spectrometer experiment: Upper atmosphere data. J. Geophys. Res, 76 2213-2227.

Beegle, L.W., Ajello, J., James, G.K., Dziczek, D., Alvarez, M. (1999), High resolution emission spectroscopy of the A $^1\Pi$ – X $^1\Pi^+$ fourth positive band system of CO excited by electron impact. Astron. Astrophys. 347, 375-390.

Bertaux, J.-L. et al. (2005), Discovery of an aurora on Mars. Nature 435, 790–794. doi: 10.1038/nature03603.

Bhardwaj, A., and S. K. Jain (2013), CO Cameron band and CO_2^+ UV doublet emissions in the dayglow of Venus: Role of CO in the Cameron band production. J. Geophys. Res. 118, 3660–3671, doi:10.1002/jgra.50345.

Bisikalo, D.V., Shematovich, V.I., Gérard, J.-C., Hubert, B. (2016), Influence of the crustal magnetic field on the Mars aurora electron flux and UV brightness, Icarus 282, 127-135.

Borst, W. L., and E. C. Zipf (1971), Lifetimes of metastable CO and N_2 molecules, Phys. Rev. A. 3, 979.

Bougher, S. W. et al. (2015), Mars Global Ionosphere-Thermosphere Model: Solar cycle, seasonal and diurnal variations of the Mars upper atmosphere. J. Geophys. Res. 120, 311–342,

doi: 10.1002/2014JE004715.

Bougher, S. W. et al (2015b), Early MAVEN Deep Dip campaign reveals thermosphere and ionosphere variability. Science 350, doi:10.1126/science.aad0459.

Bougher, S. W. et al (2016), Upper atmosphere and ionosphere, Mars 2 Book Chapter 14, Editors, B. Haberle, M. Smith, T Clancy, F. Forget, R Zurek, Cambridge University Press, in press.

Brain, D.A. et al., (2006), On the origin of aurorae on Mars, Geophys. Res. Lett. 33, L01201, doi: org/10.1029/2005GL024782.

Conway, R.R., 1981. Spectroscopy of the Cameron bands in the Mars airglow. J. Geophys. Res. 87, 4767–4775, doi:10.1029/JA086iA06p04767.

Dunseath, K. M., Fon, W. C., Burke, V. M., Reid, R. H. G., & Noble, C. J. (1997), Electron-impact excitation of the levels of carbon. J. Phys. B: Atomic, Molecular and Optical Physics 30, 277.

Erdman, P.W., and Zipf, E.C. (1983), Electron-impact excitation of the Cameron system ($a^3\Pi \rightarrow X^1\Sigma$) transition of CO. Planet. Space Sci. 31, 317–321.
doi: 10.1029/JA090iA11p11087.

Feldman, P. D., Burgh, E. B., Durrance, S. T., and Davidsen, A. F. (2000), Far-ultraviolet spectroscopy of Venus and Mars at 4 Å resolution with the Hopkins Ultraviolet Telescope on Astro-2. Ap. J. 538, 395.

Fox, J.L. (1992), Airglow and aurora in the atmospheres of Venus and Mars. In: Luhmann, J.G., Tatrallyay, M., Pepin, R.O. (Eds.), Venus and Mars: Atmospheres, Ionospheres, and Solar Wind Interactions, AGU, pp. 191–222.

Fox, J. L. (2004), CO_2^+ dissociative recombination: A source of thermal and nonthermal C on Mars. J. Geophys. Res. 109, A08306, doi:10.1029/2004JA010514.

Furlong, J.M. and Newell, W.R. (1996), Total cross section measurement for the metastable $a^3\Pi$ state of CO. J. Phys. B, 29, 331–338.

Gattinger, R. L., N. D. Lloyd, A. E. Bourassa, D. A. Degenstein, I. C. McDade, and E. J. Llewellyn (2009), Observation of the 557.7 nm to 297.2 nm brightness ratio in the auroral spectrum with OSIRIS on Odin. Can. J. Phys. 87, 1133–1137, doi:10.1139/P09-102.

Gérard, J.C., Hubert, B., Shematovich, V. I., Bisikalo, D. V., and Gladstone, G. R. (2008). The Venus ultraviolet oxygen dayglow and aurora: Model comparison with observations. Planet. Space Sci. 56, 542-552, doi: 10.1016/j.pss.2007.11.008.

Gérard, J. C., Soret, L., Libert, L., Lundin, R., Stiepen, A., Radioti, A., & Bertaux, J. L. (2015). Concurrent observations of ultraviolet aurora and energetic electron precipitation with Mars Express. J. Geophys. Res. 120, 6749-6765.

Gronoff, G. et al. (2012, Computing uncertainties in ionosphere-airglow models: II. The martian airglow. J. Geophys. Res. 117, A05309, doi: 10.1029/2011JA017308.

Gilijamse, J. J., Hoekstra, S., Meek, S. A., Metsala, M., van de Meerakker, S. Y., Meijer, G., and Groenenboom, G. C. (2007), The radiative lifetime of metastable CO ($a\ ^3\Pi$, v= 0). J. Chem. Phys. 127, 221102, doi: 10.1063/1.2813888.

Gronoff, G., C. Simon Wedlund, C. J. Mertens, M. Barthélemy, R. J. Lillis, and O. Witasse (2012), Computing uncertainties in ionosphere-airglow models: II. The Martian airglow. J. Geophys. Res. 117, A05309, doi:10.1029/2011JA017308.

Halekas, J. S., Brain, D. A., Lin, R. P., Luhmann, J. G., & Mitchell, D. L. (2008), Distribution and variability of accelerated electrons at Mars. Adv. Space Res 41, 1347-1352.

Hubert, B., Gérard, J.-C., Gustin, J., Shematovich, V. I., Bisikalo, D. V., Stewart, A. I., and Gladstone, G. R. (2010), UVIS observations of the FUV OI and CO 4P Venus dayglow during the Cassini flyby. Icarus 207, 549-557.

Itikawa, Y. (2002). Cross sections for electron collisions with carbon dioxide. J. Phys. Chem. Ref. Data 31, 749–767.

Itikawa, Y., and Ichimura, A. (1990), Cross sections for collisions of electrons and photons with atomic oxygen. J. Phys. Chem. Ref. Data 19, doi:10.1063/1.555857.

Jain, S. K., and Bhardwaj, A. (2012), Impact of solar EUV flux on CO Cameron band and CO_2^+ UV doublet emissions in the dayglow of Mars. Planet. Space Sci 63, 110-122.

James, T. C. (1971), Intensity measurements of the 0, 0 band of the a $^3\Pi$-X $^1\Sigma$ Cameron system of CO. J. Mol. Spec. 40, 545-553.

Jongma, R.T., G. Berden, and G. Meijer (1997), State-specific lifetime determination of the a $^3\Pi$ state in CO. J. Chem. Phys. 107, 7034-7040.

Keating, G. M. et al. (2008), Properties of the Mars upper atmosphere derived from accelerometer measurements, in Proceedings of 37th COSPAR Scientific Assembly 2008, Montreal, Canada, p. 1478.

Krauss, M., Neumann, D. (1975), on the interaction of O(^{1}S) with O(^{3}P). Chem. Phys. Lett. 36, 372.

Lawrence, G.M., Quenching and radiation rates of CO (a $^3\Pi$) (1971). Chem. Phys. Lett. 9, 575-577.

Leblanc, F. et al., (2006), Origins of the martian aurora observed by Spectroscopy for Investigation of Characteristics of the Atmosphere of Mars (SPICAM) on board Mars Express. J. Geophys. Res. 111, A09313. doi: 2006JA011763.

Leblanc, F. et al. (2008), Observations of aurorae by SPICAM ultraviolet spectrograph on board Mars Express: Simultaneous ASPERA-3 and MARSIS measurements. J. Geophys. Res. 113, A08311, doi: org/10.1029/2008JA013033.

Lilensten, J., Bernard, D., Barthélémy, M., Gronoff, G., Wedlund, C. S., and Opitz, A. (2015),

Prediction of blue, red and green aurorae at Mars. Planet. Space Sci. 115, 48-56.

Lundin, R. et al. (2006) Plasma acceleration above martian magnetic anomalies. Science 311, 980–983, doi :org/10.1126/science.1122152.

Millour, E. et al. (2014), The MCD/GCM Development Team, "The Mars Climate Database, MCD version 5.1," in Eighth International Conference on Mars (Lunar and Planetary Institute, Houston, TX, 2014), no. 1791, p. 1184.

Mumma, M. J., E. J. Stone, W. L. Borst, and E. C. Zipf (1972), Dissociative Excitation of Vacuum Ultraviolet Emission Features by Electron Impact on Molecular Gases. III. CO_2. J. Chem. Phys. 57, 68-75.

Paxton, L. J. (1985). Pioneer Venus Orbiter ultraviolet spectrometer limb observations: Analysis and interpretation of the 166- and 156-nm data. J. Geophys. Res. 90, 5089-5096.

Porter, H. S., and F. W. Jump (1978), Analytic total and angular elastic electron impact cross sections for planetary atmospheres, *Tech. Rep. CSC/TM-6017*, Goddard Flight Cent., Greenbelt, Md.

Porter, H.S., F. Varosi, and H.G. Mayr (1987), Iterative solution of the multistream electron transport equation, 1, Comparison with laboratory beam injection experiments. J. Geophys. Res. 92, 5933.

Schneider, N. M. et al. (2015), Discovery of diffuse aurora on Mars. Science 350, doi: 10.1126/science.aad0313.

Shematovich, V. I., D. V. Bisikalo, and J.-C. Gérard (1994), A kinetic model of the formation of the hot oxygen geocorona: 1. Quiet geomagnetic conditions. J. Geophys. Res. 99, 23,217–23,228, doi:10.1029/94JA01769.

Shematovich, V. I., D. V. Bisikalo, J.-C. Gérard, C. Cox, S. W. Bougher, and F. Leblanc (2008), Monte Carlo model of electron transport for the calculation of Mars dayglow emissions. J. Geophys. Res. 113, E02011, doi:10.1029/2007JE002938.

Shirai, T., Tabata, T., Tawara, H. (2001). Analytic cross sections for electron collisions with CO, CO_2, and H_2O relevant to edge plasma impurities. Atom. Data Nucl. Data Tables, 79, 143–184.

Simon, C., Witasse, O., Leblanc, F., Gronoff, G., & Bertaux, J. L. (2009), Dayglow on Mars: Kinetic modelling with SPICAM UV limb data. Planet. Space Sci.v57, 1008-1021.

Slanger, T. G., and Black, G. (1971), CO (a $^3\Pi$), Its production, detection, deactivation, and radiative lifetime. J. Chem. Phys. 55, 2164-2173.

Slanger, T.G., Black, G. (1981), Quenching of O(^{1}S) by O_2($a^1\Delta_g$). Geophys. Res. Lett. 8, 535–538, doi:10.1029/GL008i005p00535.

Slanger, T. G., P. C. Cosby, B. D. Sharpee, K. R. Minschwaner, and D. E. Siskind (2006), O(^{1}S→^{1}D, ^{3}P) branching ratio as measured in the terrestrial nightglow. J. Geophys. Res. 111, A12318, doi:10.1029/2006JA011972.

Soret, L., Gérard, J. C., Libert, L., Shematovich, V. I., Bisikalo, D. V., Stiepen, A., Bertaux, J. L. (2016), SPICAM observations and modeling of Mars aurorae. Icarus, 264, 398-406.

Strickland, D. J., Thomas, G. E., & Sparks, P. R. (1972). Mariner 6 and 7 ultraviolet spectrometer experiment: Analysis of the OI 1304 Å and 1356 Å emissions. J. Geophys. Res., 77, 4052-4068.

Taylor, G. W. and Setser, D. W. (1973), Quenching rate constants for CO ($a^3\Pi$; v'= 0, 1, 2). J. Chem. Phys. 58, 4840-4851.

Thomas, G. E. (1971). Neutral composition of the upper atmosphere of Mars as determined from the Mariner UV spectrometer experiments. J. Atmos. Sci. 28, 859-868.

Wauchop, T. S. and Broida, H. P. (1972). Lifetime and quenching of CO ($a^3\Pi$) produced by recombination of CO_2 ions in a helium afterglow. J. Chem. Phys. 56(1), 330-332.

Wysong, I.J. (2000), Measurement of quenching rates of CO ($a^3\Pi$, v = 0) using laser pump-

and-probe technique. Chem. Phys. Letters 329, 42-46.

Yoshino, K., J. R. Esmond, Y. Sun, W. H. Parkinson, K. Ito, and T. Matsui (1996), Absorption cross section measurements of carbon dioxide in the wavelength region 118.7–175.5 nm and the temperature dependence. J. Quant. Spectrosc. Radiat. Transfer 55, 53– 60.

TABLE 1: List of excitation processes and emission features

Excitation process	Emission	Cross section
1. $CO_2 + e \rightarrow CO_2^+(B^2\Sigma u) + e + e$	UV doublet	Shirai et al. (2001)
2. $CO_2 + e \rightarrow CO_2^+(A^2\Pi) + e + e$	FDB bands	Shirai et al. (2001)
3. $CO_2 + e \rightarrow CO(a\ ^3\Pi) + O + e$	Cameron bands	Shirai et al. (2001)*
4. $CO + e \rightarrow CO(a\ ^3\Pi) + e$	Cameron bands	Shirai et al. (2001)
5. $CO_2 + e \rightarrow CO(A^1\Pi) + O + e$	4^{th} Positive bands	Shirai et al. (2001)
6. $CO + e \rightarrow CO(A^1\Pi) + e$	4^{th} Positive bands	Shirai et al. (2001)*
7. $O + e \rightarrow O(^3S) + e$	OI 130.4 nm	Itikawa & Ichimura (1990)
8. $CO_2 + e \rightarrow CO + O(^3S) + e$	OI 130.4 nm	Shirai et al. (2001)
9. $CO + e \rightarrow C + O(^3S) + e$	OI 130.4 nm	Shirai et al. (2001)
10. $O + e \rightarrow O(^5S) + e$	OI 135.6 nm	Ajello et al. (1971)**
11. $CO_2 + e \rightarrow CO + O(^5S) + e$	OI 135.6 nm	Mumma et al. (1972)
12. $CO_2 + e \rightarrow CO + O(^1S) + e$	OI 297.2 nm	Shirai et al. (2001)
13. $CO + e \rightarrow CO + O(^1S) + e$	OI 297.2 nm	Shirai et al. (2001)
14. $O + e \rightarrow O(^1S) + e$	OI 297.2 nm	Itikawa & Ichimura (1990)
15. $CO_2 + e \rightarrow C(^5S, ^3D°) + O_2 + e$	CI 156.1 nm, 1657 nm	Shirai et al. (2001)
16. $CO + e \rightarrow C(^5S, ^3D°) + O + e$	CI 156.1 nm, 1657 nm	Paxton (1985)
17. $C + e \rightarrow C(^5S, ^3D°) + e$	CI 156.1 nm, 1657 nm	Dunseath et al. (1997)

*Renormalized, see text

**No absolute values are available

Table 2: Dependence on electron energy of the column production rate of selected auroral emissions. The electron energy input is equal to 1 mW m^{-2} in each case. Units are 10^6 photons cm^{-2} s^{-1}.

Energy (keV)	CO_2^+ UVD	CO_2^+ FDB	CO Cameron	CO 4P	OI 130.4	OI 297.2	C 156.1	C 165.7
0.25	1127	1935	4724	535	713	728	19	38
0.70	1428	2623	5167	449	392	861	20	38
2	1280	2857	4407	312	184	866	16	31
4	1092	2689	3411	213	106	743	13	25
10	843	2258	2090	111	53	526	9	18
20	553	1503	1013	56	31	307	6	12
35	373	1024	470	29	20	166	4	8
60	284	782	248	18	15	105	3	6
100	222	613	114	11	10	54	2	5
150	164	458	56	7	6	28	2	3
200	138	389	35	5	5	18	1	3

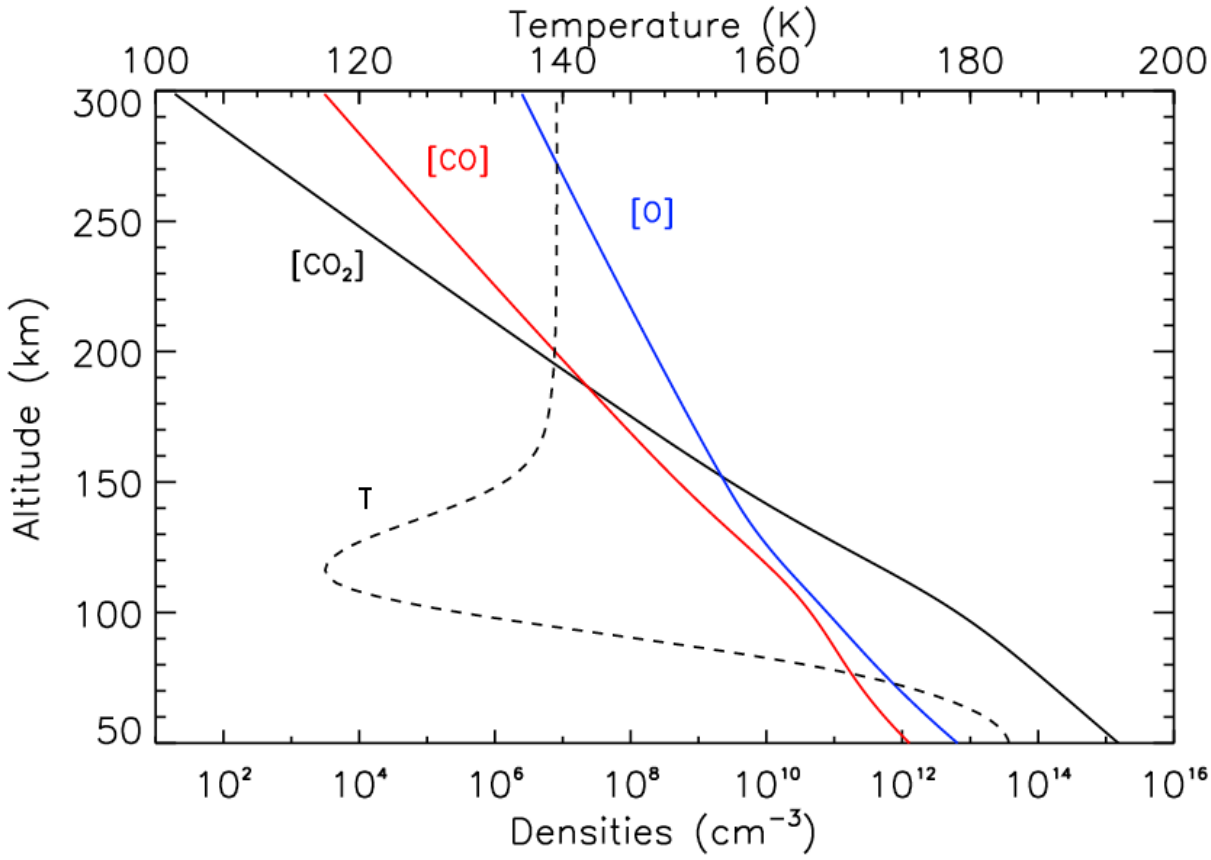

Figure 1: model atmosphere used in the Monte Carlo simulations. The temperature (top scale) and the number densities (bottom scale) were calculated by the M-GITM model with input parameters appropriate to the conditions of the diffuse aurora detection described by Schneider et al. (2015) (see text).

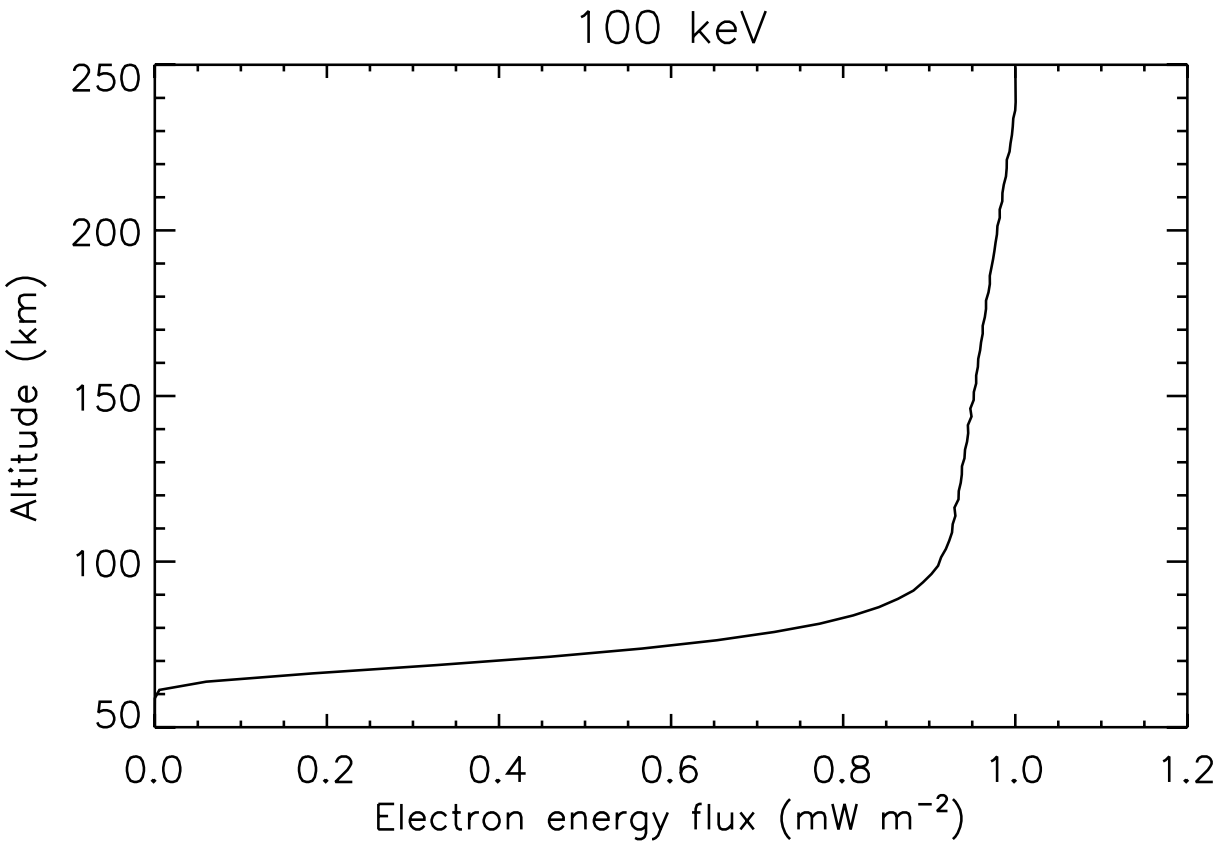

Figure 2: altitude distribution of the energy flux carried by the downward moving electrons for an initial beam of 100 keV electrons of 1 mW m^{-2} s^{-1}.

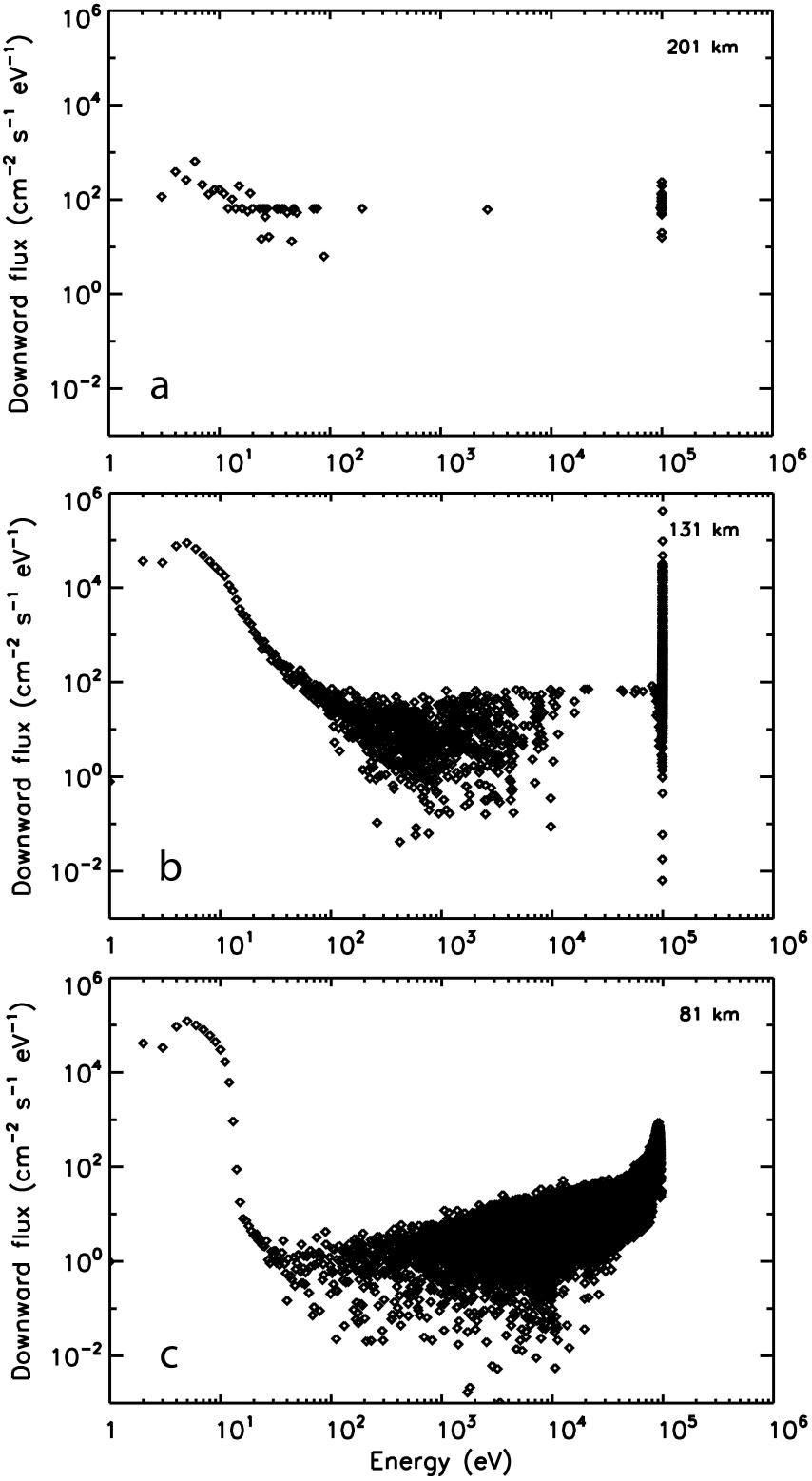

Fig. 3. Electron energy spectrum of the downward flux at 201 (top), 131 km (center) and 81 km (bottom) calculated with the Monte-Carlo electron transport model.

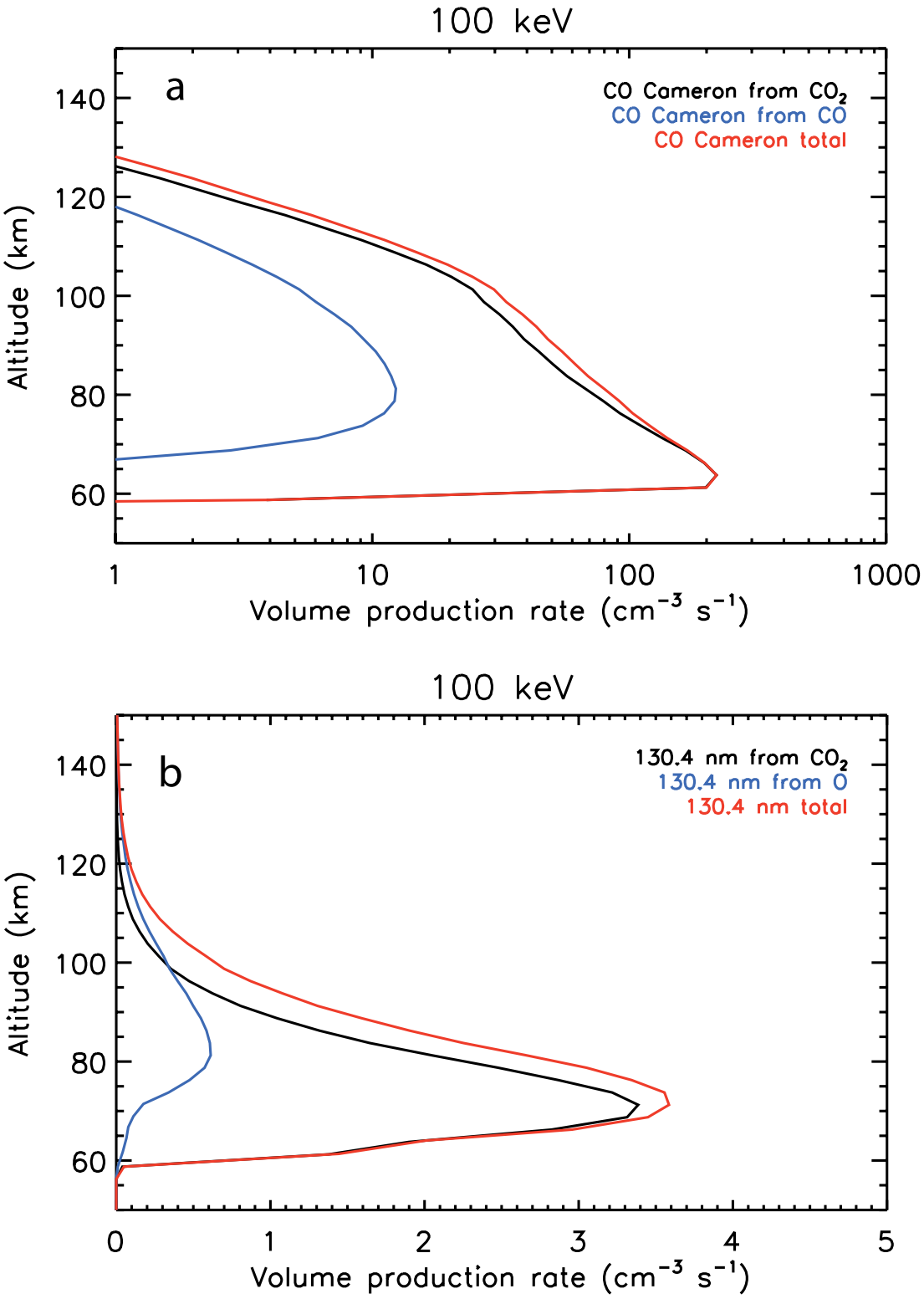

Figure 4: contributions to the volume production rate of the CO Cameron bands (a) and the OI 130.4 nm triplet (b). Excitation by electron impact on CO_2 is shown in black. The blue curves represent the contribution of electron impact on CO (a) and on O atoms (b). The red curves are the total excitation rates. The electron precipitation of 100 keV electrons carries an energy flux of 1 mW m^{-2} at the top of the model.

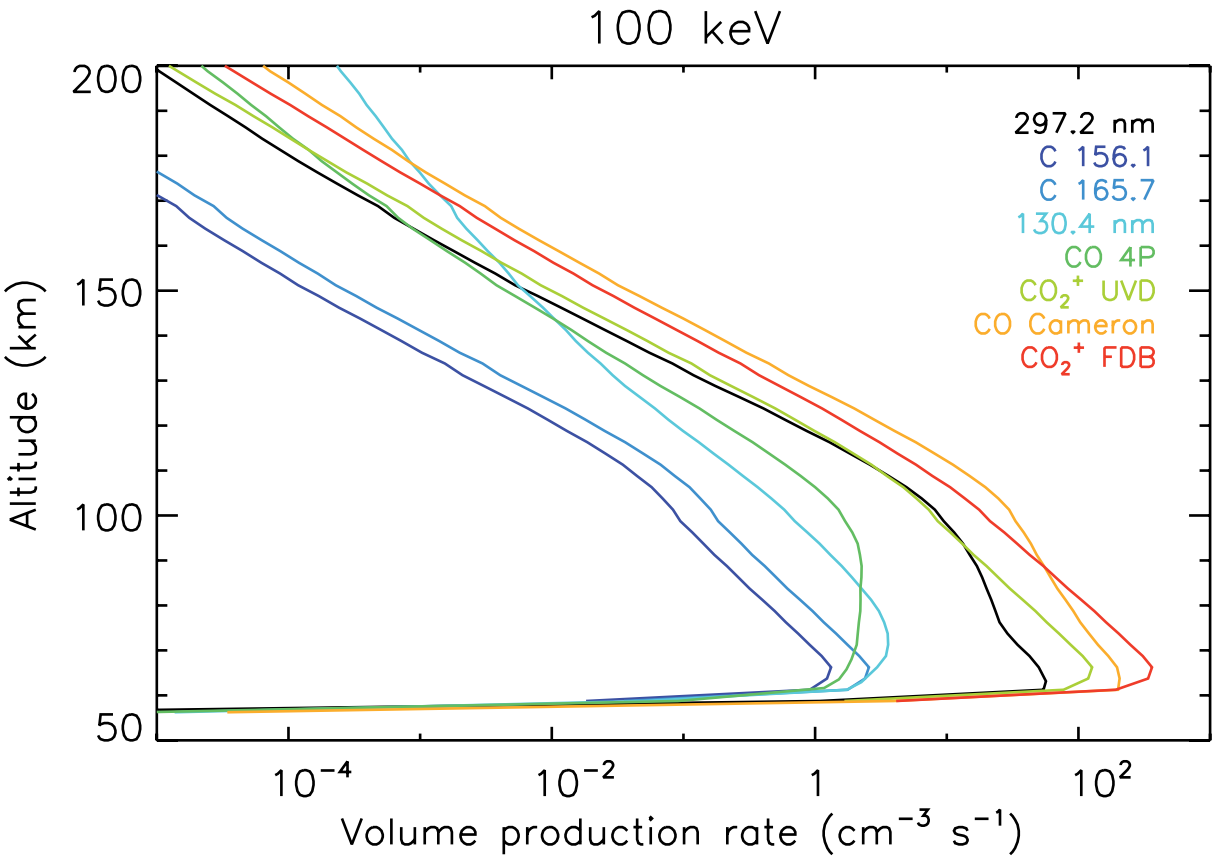

Figure 5: calculated volume production rate of selected auroral emissions for a precipitation of 100 keV electrons carrying an energy flux of 1 mW m^{-2}.

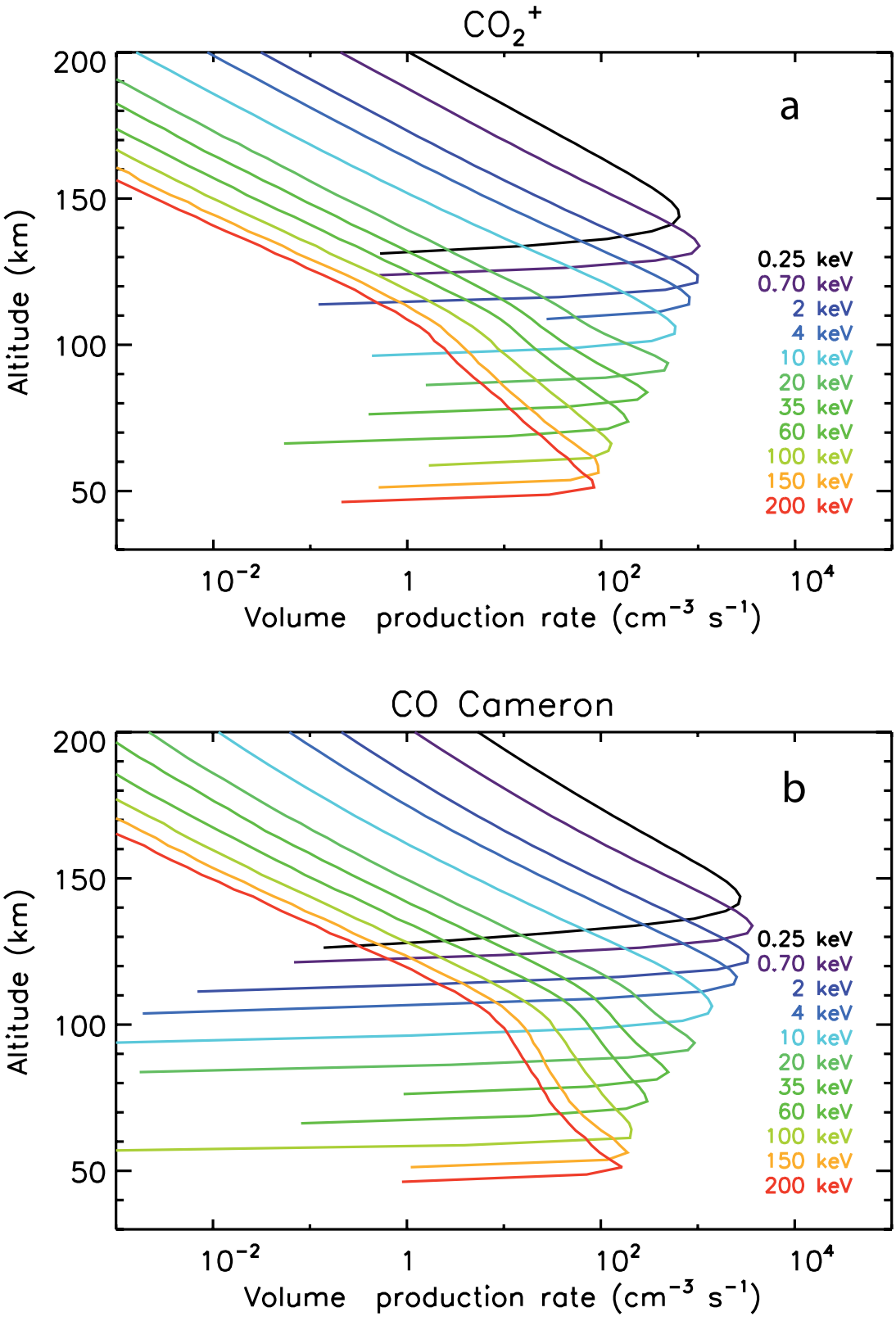

‚Figure 6: volume production rate of the CO_2^+ UVD (a) and CO Cameron (b) band emissions for different initial electron energies. The electron energy flux at the top of the model is 1 mWm^{-2} for all simulations.

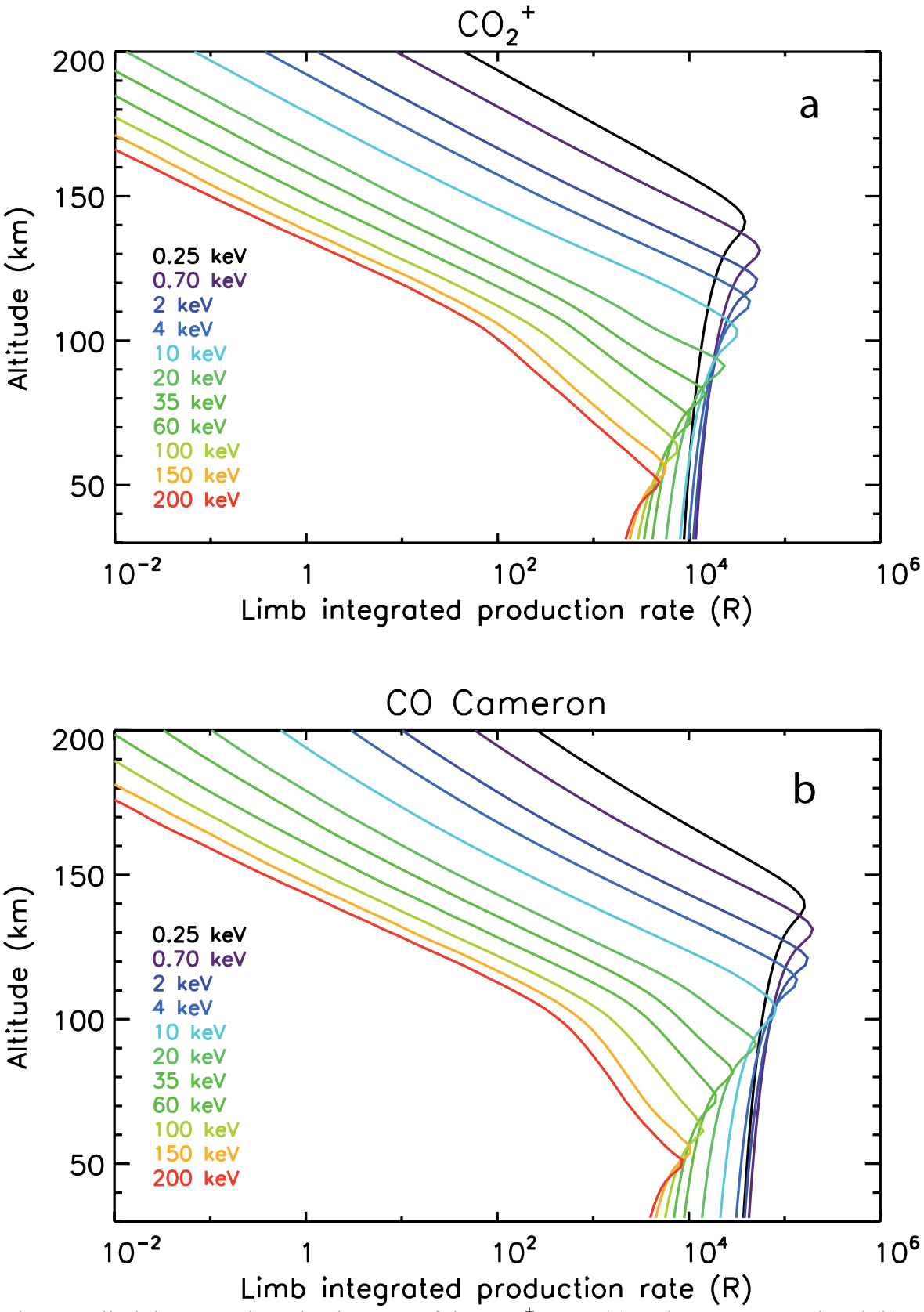

Figure 7: limb integrated production rate of the CO_2^+ UVD (a) and CO Cameron band (b) emissions for different electron energies. Quenching of the CO a state is not considered in panel (b). The electron energy flux at the top of the model is 1 mW m^{-2} for all simulations.

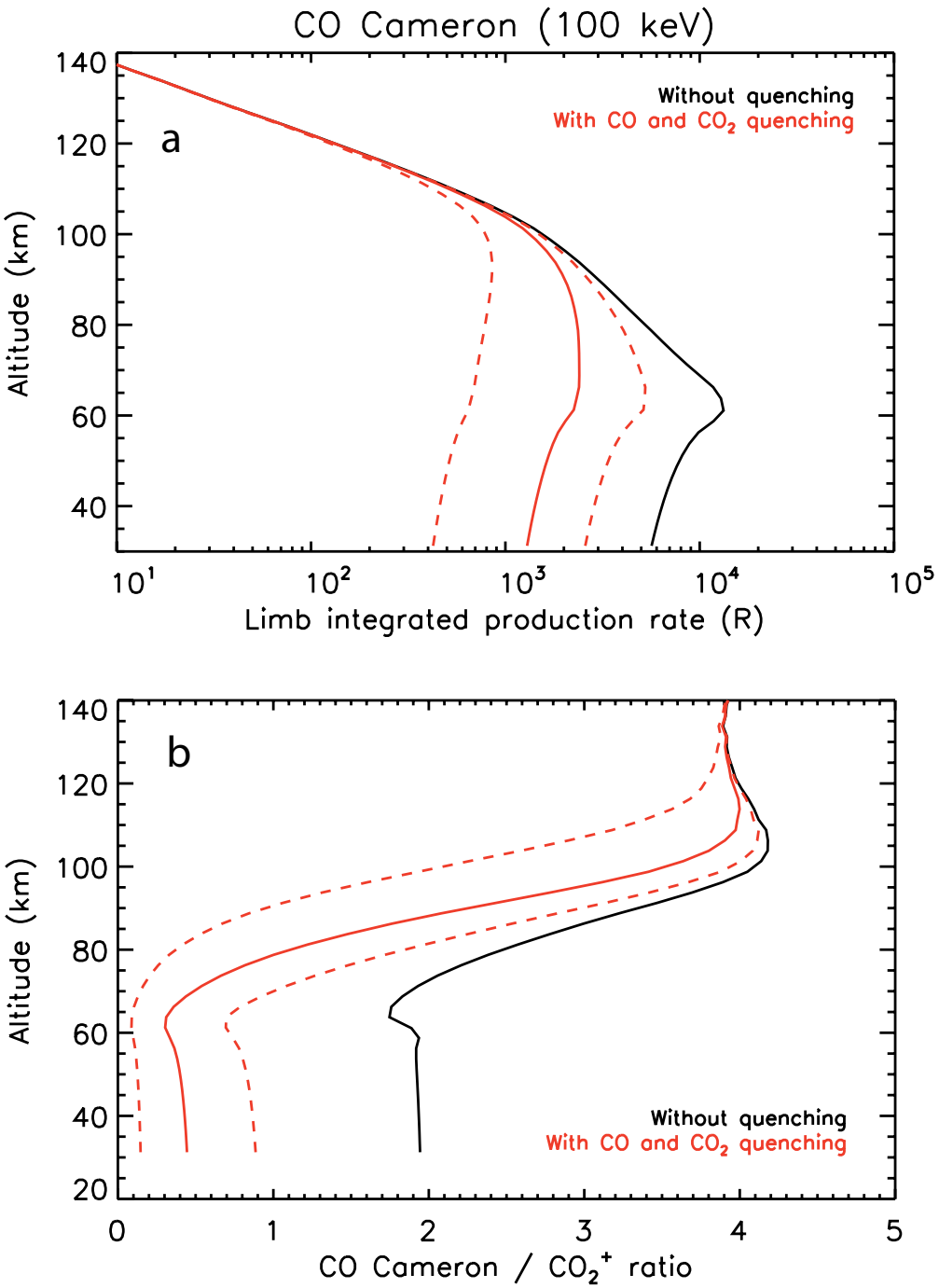

Figure 8:
(a) simulated limb profile of the Cameron band intensity without (black curve) and with (red curves) collisional quenching of the CO (a $^3\Pi$) state by CO_2 and O calculated for a precipitation of 100 keV electrons carrying an energy flux of 1 mW m^{-2}. The red solid line corresponds to the mid-range values of the quenching coefficients (see text) and the dotted lines show the range of intensities of the lifetime and quenching coefficients.
(b): simulated CO Cameron bands/CO_2^+ UVD limb intensity ratio.

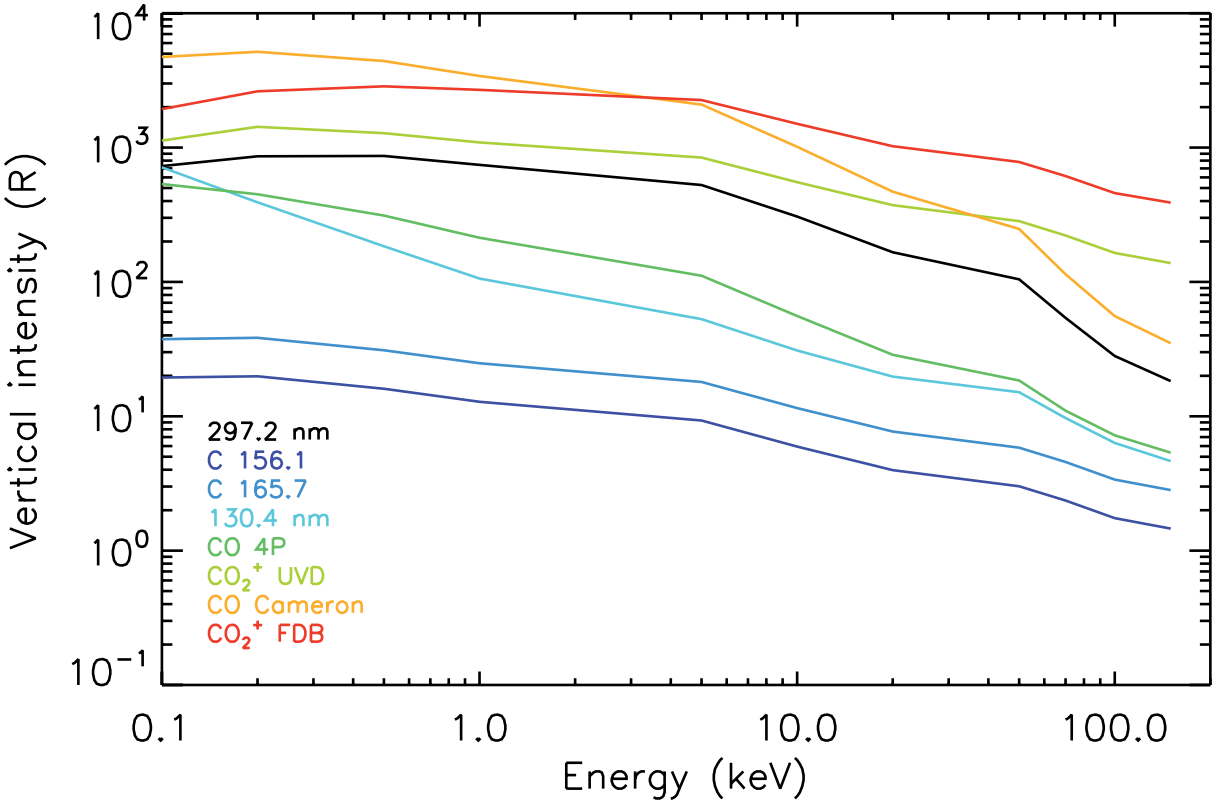

Figure 9: vertically integrated production rate of selected emissions as a function of the initial electron energy for a precipitated energy flux of 1 mW m^{-2}. Collisional quenching of the CO (a $^3\Pi$) and O(^{1}S) states has been accounted for, as discussed in section 3.5.